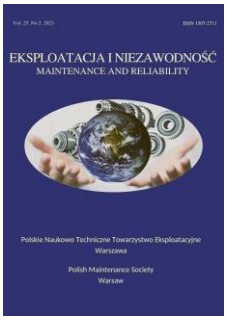

Eksploatacja i Niezawodnosc – Maintenance and Reliability

Volume 28 (2026), Issue 4

journal homepage: http://www.ein.org.pl

Article citation info:
Hu J, Yang Y, Tang L, Wang Z, Wu F, Zhou Y, Lei X, Fault diagnosis of induction motor based on current signal and EMD-MSDP-CNN, Eksploatacja i Niezawodnosc – Maintenance and Reliability 2026: 28(4) http://doi.org/10.17531/ein/218120

Fault diagnosis of induction motor based on current signal and EMD-MSDP-CNN

Indexed by: Web of Science Group

Jiao Hu[a], Yi Yang[b,*], Lun Tang[a,*], Zhi Wang[c], Fangrong Wu[a], Yihui Zhou[a], Xiping Lei[a]

[a] Collaborative Innovation Center, Hunan Automotive Engineering Vocational University, China
[b] College of Intelligence Science and Technology, National University of Defense Technology, China
[c] Tangzhi Technology Hunan Development Co., Ltd, China

Highlights

- Scattered dots and blurry edges were fixed by MSDP, improving feature extraction ability.
- The EMD-MSDP-CNN model for induction motor achieved 93.21% average accuracy.
- The experiment verified this model is effective for diagnosing weak fault current signals.

Abstract

The induction motor serves as the core power component in new energy vehicle drive systems. Any malfunction of the drive motor will directly undermine the operational reliability of the vehicle, potentially leading to drive system failures or, in severe cases, significant safety hazards endangering the lives of drivers and passengers. To address the issue of faint fault signatures within motor current signals, an image-based fault characterization method synergized empirical mode decomposition (EMD) with modified symmetrized dot pattern (MSDP) was proposed. Subsequently, a dedicated convolutional neural network (CNN) architecture with automated image feature extraction capabilities was engineered to classify motor health conditions, including healthy operation, bearing fault, and rotor broken bar. Finally, the efficiency and precision of the EMD-MSDP-CNN model for induction motor fault diagnosis were validated through experimental data, demonstrating a robust average diagnostic accuracy of 93.21% across diverse fault scenarios under multiple operating conditions.

Keywords
vehicle induction motor, current characteristics analysis, fault diagnosis, MSDP, CNN

1. Introduction

The drive system of new energy vehicles is the primary power source for vehicle operation, forming the fundamental guarantee for normal driving, energy efficiency, and driving safety. This integrated system typically includes power batteries, drive motors, motor controllers, and transmission mechanisms. As the core execution component of this system, drive motors undertake the key responsibility of converting electrical energy into mechanical energy to drive vehicle operation, directly affecting power performance and driving range. Motor failures will immediately lead to reduced vehicle power performance, abnormal driving states, and even sudden loss of power, seriously threatening driving safety and user travel experience. Such operational risks require strict technical condition monitoring of drive motors throughout the entire vehicle lifecycle—from daily use to regular maintenance—enabling early fault detection and prevention of catastrophic failures.

(*) Corresponding author.
E-mail addresses: J. Hu (ORCID: 0000-0001-8485-3147) hujiaonudt@163.com, Y. Yang (ORCID: 0000-0002-3430-557X) turbineyy@163.com, L. Tang (ORCID: 0009-0000-5614-5813) yvhygatb@163.com, Z. Wang (ORCID: 0009-0008-5677-2807) wz07600@163.com, F. Wu (ORCID: 0009-0004-3901-8766) 565039551@qq.com, Y. Zhou (ORCID:0009-0008-0206-9833) vipzhouyihui@126.com, X. Lei (ORCID: 0009-0001-0324-2430)15874186155@qq.com.

These practical demands highlight the urgent need for advanced diagnostic technologies and predictive maintenance systems, especially for induction motors, which are widely used in new energy vehicles due to their high efficiency, compact structure, and reliable performance. Research on intelligent monitoring systems integrating fault detection and residual service life prediction algorithms has become a key priority to improve the operational reliability, safety, and durability of new energy vehicles in the automotive engineering field.

Induction motors are mainly composed of three key components: stator, support bearings, and rotor, and their failure modes are mainly divided into two categories: mechanical failures and electrical failures. Bearing failure is the main form of mechanical failure in induction motors, accounting for approximately 41% of all failure types, and is usually manifested as surface fatigue damage. This is particularly prominent in new energy vehicles, as the motors operate under frequent start-stop cycles, rapid acceleration and deceleration, and variable-load conditions, which exacerbate bearing wear and fatigue. Electrical failures of induction motors mainly include stator faults and rotor faults. Stator faults account for about 37% of all induction motor faults [1], with the main manifestation being interturn short circuits. Interturn short circuits occur due to the aging and failure of coil insulation windings, and their formation reasons are relatively complex, mainly summarized as follows: (1) During the motor start-stop process, the stator insulation material withstands significant transient overvoltage; (2) When the motor operates at an excessively high temperature, the insulation material bears substantial thermal stress; (3) Minor vibrations during operation cause damage to the interturn insulation material. Rotor faults are also an important type of induction motor failure, accounting for about 10% of all fault types [2,3]. The main manifestation of induction motor rotor faults is rotor broken bars. During the operation of new energy vehicles, induction motors are subjected to the alternating effects of electromagnetic force, centrifugal force, thermal stress, and mechanical stress—compounded by rotor manufacturing defects, machining and assembly errors, and the impact of variable working conditions—making rotor bars prone to fatigue and fracture. Once a rotor broken bar occurs in an induction motor, the overall performance of the new energy vehicle will be significantly affected, manifesting as reduced driving power, increased energy consumption, unstable speed, and abnormal noise during operation.

In recent years, a large number of fault diagnosis research results have emerged with motors as the object. Niu et al. [1] summarized the diagnosis criteria of typical induction motor defects including bearing faults, interturn short circuits, rotor broken bars, and delineated various fault diagnosis methodologies rooted in current signal analysis, encompassing the demodulation transforms, parameter estimation, and artificial intelligence algorithms. Mina et al. [4,5] proposed a fast detection method by obtaining current envelope signals through the Hilbert transform and statistical parameter estimation. Zawad et al. [6] evaluated and analyzed the performance of 17 classifiers on induction motor fault types using matched tracking and discrete wavelet transform for feature extraction. Abderrahim et al. [7] have introduced a technique that involves the use of a current-normalized residual harmonic analysis as a diagnostic tool for identifying interturn short circuits and rotor broken bar in induction motors. Zhang et al. [8] proposed to determine the change in mutual inductance through the fault current in a quantitative model, and estimated the change in air gap length curve through a transfer function to measure bearing fault severity. Gao et al. [9] obtained missing fault samples through a finite element model, and used a generative adversarial network to further generate more fault samples. These expanded fault samples enabled the classifier to exhibit better classification performance. Lannoo et al. [10] improved an air gap permeability expression that can be interpreted at the physical level and is easily derived according to rotor position, which can quickly obtain magnetic equivalent circuits close to finite element accuracy. Gong et al. [11] developed a multichannel deep convolutional neural network capable of combining the vibration and current signals of motors to learn the composite fault characteristics, and experimentally verified the model stability and effectiveness. Roy et al. [12] investigated a method for real-time bearing fault diagnosis in induction motors, which is grounded in the theory of differential visualization. Focusing on the starting transient current of induction motors, Martinez-Herrera et al. [13] distinguished between bearing outer ring fault and other faults in experimental signals though training a neural network model

based on the transient current characteristics obtained from the analysis of current signal uniformity and kurtosis. Targeting the low signal-to-noise ratio (SNR) traits of bearing faults, Ma. del Rosario et al. [14] employed a phase-locked amplifier to lock the fault characteristic frequency of transmission bearing solving the interference problem of other vibration sources in the acoustic signal environment. Zhu et al. [15] developed a CNN with multiscale feature fusion architecture to extract multidimensional features of rotor defects in induction motors. Integrating the global and local features of the current signals, Vu et al. [16] constructed a double-branch model to respectively obtain the relationships between query set, support set and signal features, and performed fault feature fusion at the end of the branch. Dong et al. [17] applied a strategy for ITSC detection and fault phase identification using only stator voltage signals in order to overcome the effects of fault feature confusion and non-smooth conditions generated by unbalanced voltage. Purbowaskito et al. [18] explored a approach using a state space model to overcome the disadvantages of the low SNR of current signal and the fault features being easily obliterated by the harmonics and noise. To overcome the limitation of easily filtering fractional chaotic information in nonlinear vibration signals, Song et al. [19] proposed an improved two-dimensional multi-scale fractional dispersion entropy approach for rolling bearing faults classification.

According to the literature research mentioned above, the current diagnostic implementation process for motor faults mainly consists of three stages: state perception, signal processing, and fault diagnosis. During the state perception phase, the primary types of detectable signals that have been developed encompass vibrations, electrical current, magnetic flux, and acoustics, among others. Due to low acquisition cost, no need to approach the motor body and ease integration with the control system, the research on current signals has received widespread attention for fault diagnosis. At the signal processing stage, The primary focus lies in addressing how to enhance fault signatures to facilitate fault type identification. The key challenges stem from the inherent characteristics of sensed fault signals: low signal intensity and poor signal-to-noise ratio (SNR). During spectral analysis, these signals are particularly vulnerable to fundamental frequency spectral leakage and power line interference, which collectively result in compromised effectiveness of fault feature extraction. In the fault recognition stage, the methods mainly include data-driven and model-based fault identification methods. Model-driven fault identification approaches offer advantages including minimal training sample requirements, avoidance of costly fault testing procedures, and enhanced interpretability through physics-based formulations with clear fault mechanisms. However, they face critical limitations in developing high-fidelity models that accurately capture system dynamics, and persistent deviations between constructed models and actual systems caused by unquantifiable external disturbances resistant to precise evaluation. The rapid advancement in computational capabilities coupled with the widespread proliferation of deep learning methodologies has significantly propelled the extensive implementation of data-driven artificial intelligence algorithms in fault diagnostic applications across industrial systems.

Hence, this paper studied an image-based fault detection method using EMD-MSDP-CNN for the weak fault characteristics in induction motor current signals. Firstly, EMD was utilized to remove the dominant power frequency components and their harmonics from the decomposed current signal. Secondly, the SDP methodology was applied to transform the time-domain current into the polar coordinate space, and the correlation window constraints were added to form the MSDP method to reduce the effect of the discrete isolated dots during the mapping process of the weak signals. Thirdly, a multi-layer CNN was built to self-extract features from the polar coordinate image mapped by the weak current signals. Finally, the fault diagnosis results using EMD-MSDP-CNN model were compared with those of multiple classical intelligent models based on the experimental data, which affirmed the validity and accuracy of the proposed approach for the typical faults identification of the induction motors.

2. Methodological framework

2.1. Preprocessing of de-power frequency based on EMD

In an ideal scenario, an induction motor operates as a balanced mechanical-electrical-magnetic system, characterized by three-phase current of uniform amplitude and circumferentially equidistant phase angles. The occurrence of a fault within the motor's structure induces variability in its physical attributes,

such as the current, frequency, noise and vibration, torque, etc, thereby compromising the equilibrium of the motor's operational parameters. The presence of asymmetry in three-phase current serves as a diagnostic indicator of faults within the motor, as evidenced by the phase currents. Empirical evidence has substantiated the assertion that any given three-phase current configuration can be resolved into a set of positive-sequence, negative-sequence, and zero-sequence components, as depicted in Fig. 1. Under ideal symmetry condition, the magnitudes of the last two components are nil due to the inherent symmetry of the three-phase system, implying the exclusive existence of positive-sequence components. From a theoretical perspective, a three-phase system afflicted by a fault is in a disequilibrium state, which can identify non-negligible negative-sequence and zero-sequence components through decomposition.

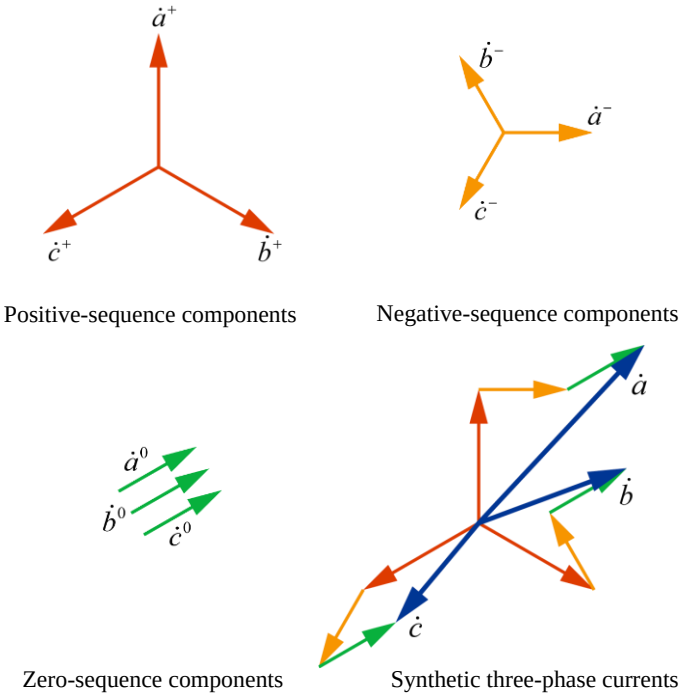

Positive-sequence components | Negative-sequence components

Zero-sequence components | Synthetic three-phase currents

Figure 1. Three-phase currents decomposition.

In practical applications, absolute symmetry of motor parameters is almost impossible to achieve, and the negative-sequence and zero-sequence components always exist objectively, i.e. numerically non-zero. In addition to the asymmetry of the motor parameters, the motor fault is also reflected in the aforementioned components. Besides, the three-phase current often do not strictly differ by 120° due to the power supply quality issues of the frequency converter, and the synthetic zero-sequence current inevitably carries the power frequency and its multiplier, which needs to be eliminated.

EMD constitutes an adaptive approach to time-frequency signal processing, which is particularly adept at handling non-stationary and nonlinear signals [20]. This method facilitates the decomposition of signals into a discrete set of intrinsic mode functions (IMFs), each capturing the local temporal features of the signal at distinct time scales. Hence, EMD is utilized to mitigate the impact of power frequency and its harmonics on zero-sequence current. The theoretical framework and the detailed decomposition procedure associated with EMD can be referred to references [20].

2.2. Modified Symmetrized Dot Pattern

The SDP method was initially presented and utilized to the visual representation of language signals [21]. Different from conventional time-frequency analysis, this approach converts one-dimensional normalized time-domain waveforms to symmetrical dots, thus creating two-dimensional scatter plots on polar coordinate involved in the amplitude-frequency characteristics and distribution of the time-domain signals, which presents a new viewpoint for fault diagnosis in a more intuitive visual processing. Its basic principle and specific definition are shown in Fig. 2 and Eq. (1), respectively [21].

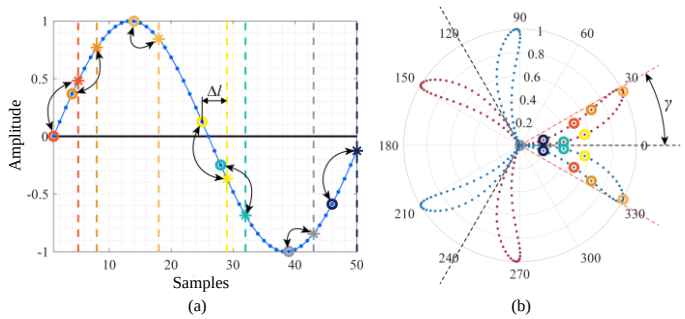

Figure 2. The SDP conversion principle. (a) Time domain; (b) Polar coordinate domain.

$$\begin{aligned} r(i) &= \frac{x_i - \min(x)}{\max(x) - \min(x)}, \\ \Theta(i) &= \gamma_0 + \frac{x_{i+\Delta l} - \min(x)}{\max(x) - \min(x)}\gamma, \\ \Phi(i) &= \gamma_0 - \frac{x_{i+\Delta l} - \min(x)}{\max(x) - \min(x)}\gamma, \end{aligned} \tag{1}$$

where x is the raw signal, r is the radius in polar coordinates, i represents the ith sampling point, Θ / Φ are the counterclockwise/clockwise deflection angle relative to the plane of mirror symmetry. $\Delta l/\gamma_0/\gamma$ are the delay coefficient/rotation angle of the mirror symmetric plane/deviation angle gain, respectively.

During signal processing, it is found that minority samples have several outlier dots that significantly deviate from the general position due to the low SNR zero-sequence current, which causes the instability of the scattering dot concentration region of the classical SDP in the radial range. Therefore, the MSDP method is proposed to limit the oscillating range of the scattering dot concentration region through the dimension adjustment of computational point correlation window, avoiding the adaptability influence of directly removing outliers on the SDP. Hence, Eq. (1) is revised as follows:

$$\begin{aligned} X(i) &= \left\{x_j | i - \frac{H}{2} \le j \le i + \frac{H}{2}, j \in \mathbb{N}^+\right\}, \\ r_{\mathrm{L}}(i) &= \frac{x_i - \min[X(i)]}{\max[X(i)] - \min[X(i)]}, \\ \Theta_{\mathrm{L}}(i) &= \gamma_0 + \frac{x_{i+\Delta l} - \min[X(i)]}{\max[X(i)] - \min[X(i)]}\gamma, \\ \Phi_{\mathrm{L}}(i) &= \gamma_0 - \frac{x_{i+\Delta l} - \min[X(i)]}{\max[X(i)] - \min[X(i)]}\gamma, \end{aligned} \tag{2}$$

where H/L are the window/sample length, $X(i)$ is the collection of all sample points within the ith sample point window, and $i \in \left[1 + \frac{H}{2}, L - \frac{H}{2}\right]$.

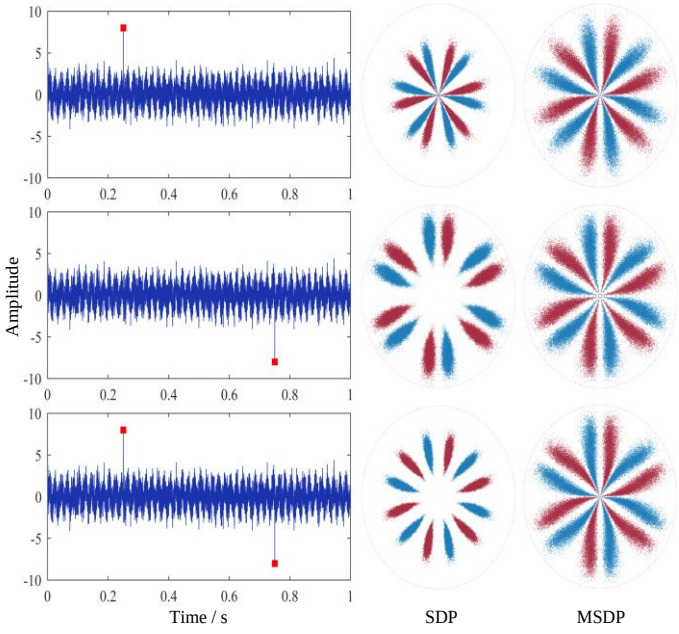

Figure 3. The effects comparison of outliers on SDP and MSDP.

A noisy signal $f(t) = sin(2\pi \cdot 50 \cdot t) + N(0,1)$is used to simulate zero sequence current, where N represents Gaussian noise with mean and standard deviation of 0 and 1, respectively. Then, the deviation value are inserted into the noise signal. Currently, there is still a lack of established methods in existing literature to determine appropriate model parameters, the trial-and-error method is still the most direct way to obtain stable patterns. Most studies employing SDP for the analysis of vibration and acoustic signals indicate that the value of the delay coefficient should not exceed 10 [22], so with parameters set as $\Delta l = 10, \gamma_0 = 45°, \gamma = 30°, H = L/8$, the abovementioned two modes are utilized to perform signal conversion. Fig. 3 shows the effects of different outliers on SDP and MSDP, respectively. The results demonstrate that the scatter distribution of SDP deviates significantly due to outliers interference, and outliers at different positions cause large fluctuations in the scatter distribution, while the MSDP method effectively mitigates this impact.

2.3. Modified Symmetrized Dot Pattern

CNN is an architecture characterized by a multi-layer deep learning model. It is constructed through the sequential interplay of convolutional and downsampling layers, which are subsequently linked to one or more fully connected layers, culminating in an output layer that yields the classification outcomes of image features. The network architecture is depicted in Fig. 4. The fundamental principle underlying this methodology is to cut down the free parameters and computational complexity via the employment of local receptive fields and the sharing of neuron weights, which could enhance the network's computational efficiency. Meanwhile, the input data features (images) can be made translation, rotation and scaling invariant due to the pooling effect of the downsampling layer.

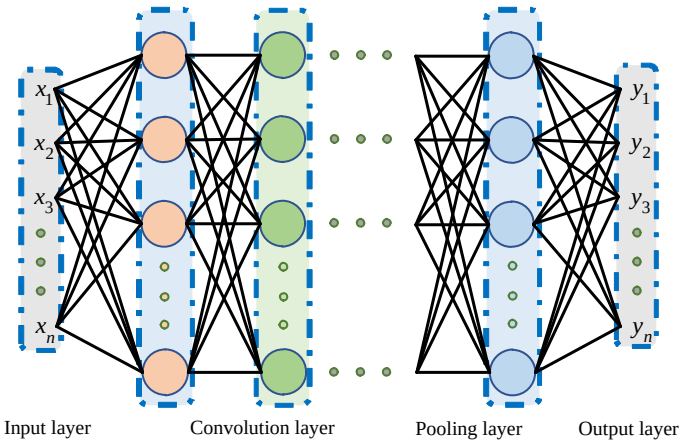

Figure 4. The sketch map of CNN.

The CNN structure constructed in this article was shown in Table 1.

Table 1. The CNN structure.

Layer	Convolutional kernel (H x W/step)	Characteristic graph
Input layer	-	300×300×3
Convolutional layer 1	3 x 3 x 64/1	304×304×64
Pooling layer 2	2×2/2	152 x 152 x 64
Convolutional Layer 3	3 x 3 x 128/1	156 x 156 x 128
Pooling layer 4	2×2/2	78 x 78 x 128
Convolutional layer 5	3 x 3 x 256/1	82×82×256
Convolutional layer 6	3 x 3 x 256/1	86×86×256
Pooling layer 7	2×2/2	43 x 43 x 256
Convolutional layer 8	3 x 3 x 512/1	47 x 47 x 512
Convolutional layer 9	3 x 3 x 512/1	51 x 51 x 512
Pooling layer 10	2×2/2	25 x 25 x 512
Convolutional layer 11	3 x 3 x 1024/1	29×29×1024
Convolutional layer 12	3 x 3 x 1024/1	33×33×1024
Fully connected layer	33×33×3	1×1×3
Output layer	-	3

Specifically, the pooling type and activation function adopt Max pooling and the ReLU function, respectively.

3. Result analysis

3.1. Experimental data

Experimental current signals of induction motor were collected from VALENIAN-PT600 motor fault test rig, which predominantly features drive motor, planetary gearbox, magnetic powder brake, current sensor, data acquisition device, etc. The main parts and parameters of the test rig are shown in Fig. 5 and Table 2.

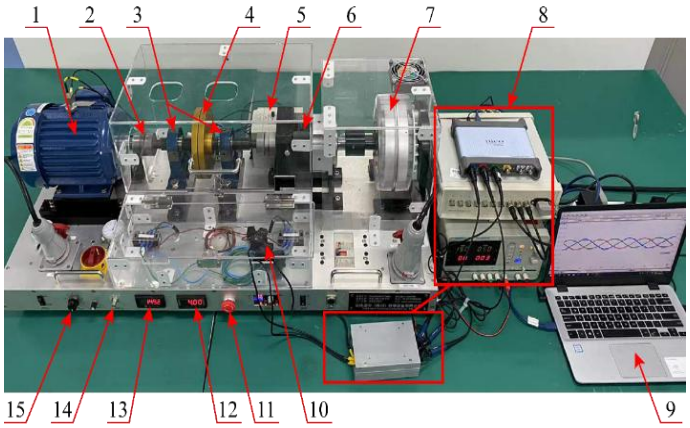

Figure 5. VALENIAN-PT600 motor fault test rig.

Due to the different operating conditions of induction motors under different load conditions, the induction motors present different fault characteristics performance. To validate the efficiency of proposed method under different running scenarios, current data were experimentally perceived in three different load conditions (no load 0 kW, half load 0.75 kW, full load 1.5 kW) and three different motor health states (normal state, bearing fault, and rotor broken bar), respectively. The rated speed of the motor is 1750 r/min. A segment of the induction motor rotor adjacent to the aluminum ring was removed, with dimensions of 45° in the circumferential direction and 15 mm in the transverse direction, to simulate the rotor broken bar fault of the motor. The wire electrical discharge machining process was adopted to implant a crack into the inner ring of bearing at the drive end of the motor, with a width of 0.3 mm and a depth of 3 mm. The fault-implanted samples are shown in Fig. 6.

Table 2. VALENIAN-PT600 Composition.

Number	Name	Quantities	Model/remarks
1	Induction motor	1	HYOSUNG HSX0704281
2	Rigid coupling	2	-
3	Bracket bearing housing	2	PH 206
4	Rotor	1	-
5	AC inverter	1	-
6	Planetary geabox	1	PGX-120
7	Magnetic powder brake	1	24V supply, torque 0-50 Nm
8	Signal acquisition and conditioning equipment	1	-
9	Computer	1	-
10	Current sensor	3	-
11	Emergency stop button	1	-
12	Current digital display	1	-
13	RPM digital display	1	-
14	RPM pulse signal interface	1	-
15	RPM control knob	1	-

Figure 6. The fault-implanted samples. (a) Rotor broken bar; (b) Bearing inner-ring fault.

As a result, a test dataset of induction motors including nine different conditions was constructed. Ten repetitive experiments were carried out at 200 kHz sampling frequency, with a single acquisition duration of 5 s. Fig. 7 illustrated a selection of current signals from induction motors under various health states.

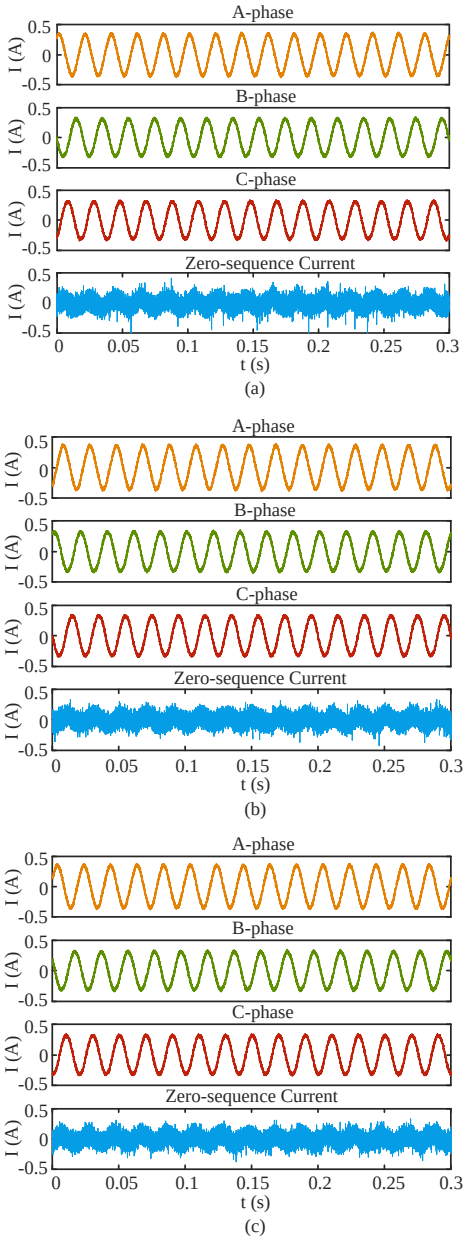

Figure 7. Three-phase currents and zero-sequence currents. (a) Normal; (b) Rotor broken bar; (c) Bearing fault.

3.2. Analysis based on SDP and MSDP methods

The current signals of the induction motor fault experiments were converted into images based on the SDP and MSDP methods respectively. Considering the research on current signals as a new object and the high sampling rate, the selection of Δl in this paper is not limited to the recommended range. Through extensive experiments, it is found that when Δl is around 1000, the distinction of image morphology reaches the optimal level and is insensitive to small-range variations. Therefore, $\Delta l = 1000$ is adopted in all subsequent studies. In addition, γ_0, γ, H are set to 60°, 30°, 4000, respectively. These image dataset included nine different conditions, and each condition contained 960 feature images. Figs. 8-9 showed some images conversion results using the SDP and MSDP methods in the nine conditions, respectively. Observing the above two sets of images, the images mapped by the SDP method had more scattered dots, leading the overall shapes and edges of images to be blurry, as shown in Fig. 8. In contrast, the mapping dots of images using the MSDP method were closer to the polar origin due to the correlation window limitation on the diffusion range, as shown in Fig. 9. Consequently, the images presented more vivid and plump, which was beneficial for the image features extraction.

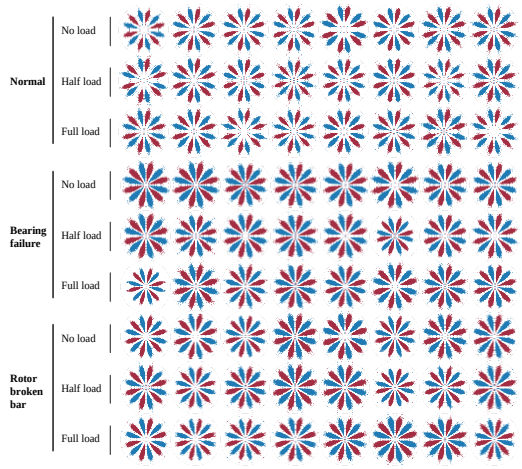

Figure 8. Partial current images of induction motor fault experiment using SDP method.

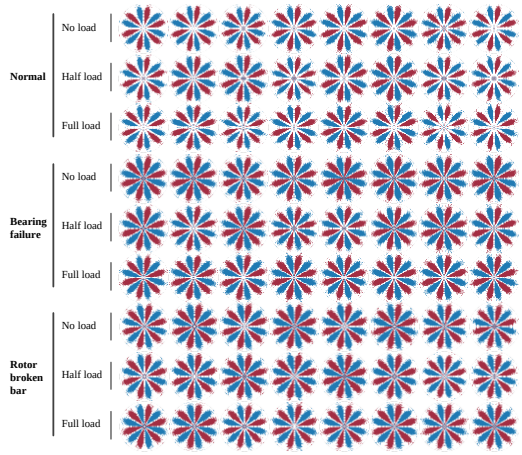

Figure 9. Partial current images of induction motor fault experiment using MSDP method.

3.3. Multi-classification fault diagnosis analysis

Taking all SDP and MSDP images as the classification object, the image samples were divided into training and testing subsets in a 7:3 ratio through stratified sampling to ensure balanced representation of all state categories. For the network model

training, the AdamW optimizer was employed, configured with a learning rate of 0.001 and a weight decay of 1e-4, while the remaining parameters were set to default values. The batch size and the number of iterations were fixed to 16 and 30, respectively. These hyperparameters were selected based on preliminary grid search optimization and early stopping validation to avoid gradient explosion or training stagnation. Figs. 10-11 illustrated the confusion matrices of the classification results using EMD-SDP-CNN and EMD-MSDP-CNN models under different load conditions, respectively. The results demonstrated that both models achieved high accuracy in identifying normal samples, with EMD-SDP-CNN yielding 99.3%, 99.0%, and 100.0% accuracy under no-load, half-load, and full-load conditions, respectively, while EMD-MSDP-CNN achieved 98.6%, 99.7%, and 98.6% under the same load conditions. However, the EMD-SDP-CNN model exhibited limitations in distinguishing bearing faults and rotor broken bar. The diagnostic accuracies of bearing fault were 72.2%, 53.1%, 75.0% under three load conditions, respectively, and the diagnostic accuracies of rotor broken bar were only 84.4%, 88.2%, 86.5%, respectively. In contrast, the EMD-MSDP-CNN model demonstrated substantial improvements, achieving 89.9%, 92.7%, 89.2% accuracies for bearing fault and 92.0%, 86.1%, 92.0% for rotor broken bar under the respective load conditions. Overall, the average diagnostic accuracies of the two typical faults increased by 23.8% and 3.6% under three load conditions, respectively. This also proves the superiority of the model proposed in this paper in terms of the accuracy of diagnosing typical fault types.

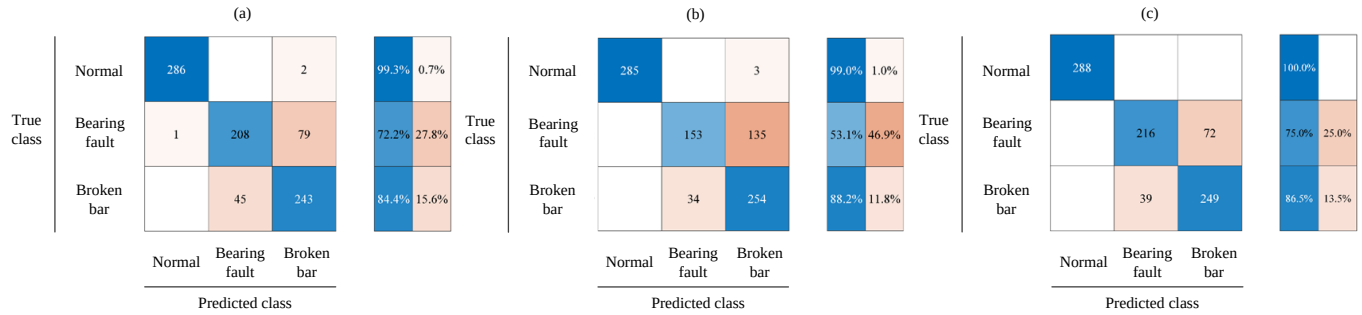

Figure 10. Multi-classification diagnostic confusion matrix using EMD-SDP-CNN. (a) No load; (b) Half load; (c) Full load.

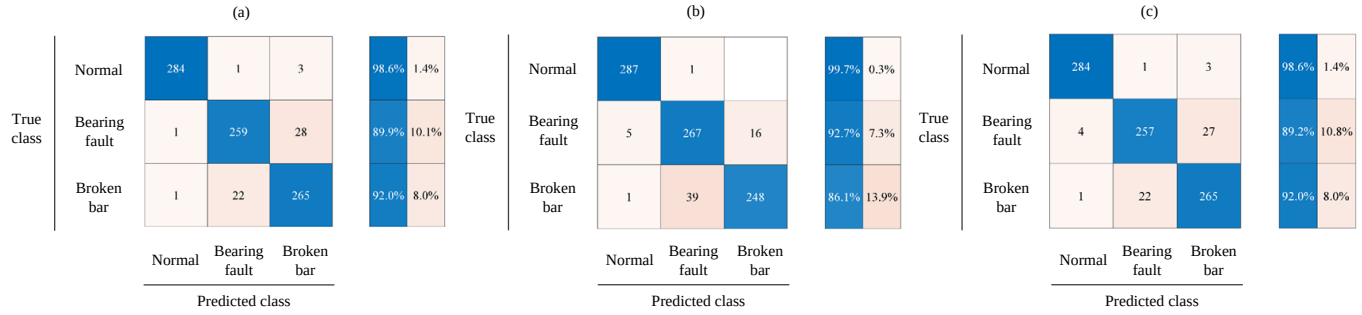

Figure 11. Multi-classification diagnostic confusion matrix using EMD-MSDP-CNN. (a) No load; (b) Half load; (c) Full load.

To verify the necessity of the model components, this paper conducted ablation experiments and compared the diagnostic performance with several typical intelligent models. The results are presented in Table 3.

As shown in Table 3, the SDP-SVM and SDP-CNN methods exhibited the poorest diagnostic performance, with average diagnostic accuracies of only 77.15% and 79.34% respectively across the three states. This is attributed to their failure to mitigate the interference caused by the power frequency and its harmonic frequencies in the zero-sequence current, which impedes the extraction of weak features. After adding the EMD preprocessing module, the diagnostic accuracies of the two models were improved to 82.58% and 84.17% respectively. By replacing SDP with MSDP to eliminate the interference of outliers in the signal, the diagnostic performances of both models were significantly enhanced, with accuracy increases of 7.27% and 9.04% respectively. Specifically, the accuracy of the EMD-MSDP-CNN model reached 93.21%, which was essentially comparable to that of the EMD-MSDP-ResNet model (93.20%). Compared with ResNet, the CNN network has

a shallower structure, making it more suitable for lightweight deployment in bearing fault diagnosis scenarios with resource constraints or high requirements for real-time diagnosis.

Table 3. Diagnosis accuracy comparison.

Methodologies	No load	Half load	Full load	Average accuracy
SDP-SVM	74.82%	79.35%	77.28%	77.15%
SDP-CNN	76.82%	81.55%	79.65%	79.34%
EMD-SDP-SVM	77.95%	85.31%	84.48%	82.58%
EMD-SDP-CNN	85.27%	80.09%	87.15%	84.17%
EMD-MSDP-SVM	89.85%	90.42%	89.94%	89.85%
EMD-MSDP-CNN	93.52%	92.82%	93.29%	93.21%
EMD-MSDP-ResNet	92.50%	93.80%	93.30%	93.20%

Therefore, the comparison of multi-class fault diagnosis results among different methods indicates that the EMD-MSDP-CNN model proposed in this paper achieves effective identification of fault types under different operating loads. This model exhibits significantly improved diagnostic robustness in complicated working conditions, outperforms other classical models in terms of average diagnostic accuracy.

The current study is limited to three typical health status (normal, bearing fault, rotor broken bar) and load conditions (0 kW, 0.75 kW, 1.5 kW). The generalizability of the proposed model to other fault modes (e.g., stator interturn short circuits) or variable operating environments (e.g., variable speed or transient states) requires further investigation. Secondly, the key parameters in the MSDP were obtained through a trial-and-error method. In subsequent work, intelligent optimization algorithms can be employed to further enhance the rationality of parameter settings. Similarly, the hyperparameters such as network structure parameters, convolutional layer parameters, and training parameters in CNN model can also be optimized through intelligent algorithms to continuously improve diagnostic accuracy. Future research will focus on expanding fault categories and complex operating conditions, verifying the adaptability of the model's diagnosis in industrial scenarios, continuously improving diagnostic accuracy through intelligent optimization of model parameters, and balancing model performance, resources, costs, and real-time requirements to meet the operation and maintenance needs of industrial sites.

4. Conclusions

This paper focuses on bearing faults and rotor broken bars occurring during the operation of new energy vehicle induction motors. Building on signal processing and coordinate space transformation techniques, this study investigates current-based image feature extraction for induction motors, identifying diagnostic characteristics with high accuracy and strong applicability. Leveraging deep learning's powerful nonlinear representation capability for complex signals, a multi-classification fault diagnosis method based on EMD-MSDP-CNN is proposed. The validity and accuracy of the proposed model are experimentally verified using a motor fault simulation platform. This methodology is expected to provide solutions for the condition perception and intelligent diagnosis of induction motors, and offer model- and algorithm-level technical support for improving the scientific maintenance and protection of critical power components in new energy vehicles. In the future, the research will further focus on the variable operating conditions of vehicles, expand the diagnostic accuracy and robustness of the model under complex conditions such as sudden load changes and speed fluctuations, optimize the feature extraction algorithm to adapt to the signal characteristics under multiple operating conditions, and provide reliable technical support for the full-condition intelligent fault diagnosis of power systems in new energy vehicles.

Acknowledgment

This work was financially supported by the Natural Science Foundation of Hunan Province of China (Grant No. 2024JJ8096).

References

1. Niu G, Dong X, Chen Y. Motor Fault Diagnostics Based on Current Signatures: a Review, IEEE Transactions on Instrumentation and Measurement 2023; 72: 3520919. https://doi.org/10.1109/TIM.2023.3285999.
2. Mehrjou M R, Mariun N, Marhaban M H, Misron N. Rotor fault condition monitoring techniques for squirrel-cage induction machine-A review, Mechanical Systems and Signal Processing 2011; 25(8): 2827–2848. https://doi.org/10.1016/j.ymssp.2011.05.007.
3. Bellini A, Filippetti F, Tassoni C, Capolino G A. Advances in Diagnostic Techniques for Induction Machines, IEEE Transactions on Industrial Electronics 2008; 55(12): 4109–4126. https://doi.org/10.1109/TIE.2008.2007527.
4. Abd-El-Malek M, Abdelsalam A K, Hassan O E. Induction motor broken rotor bar fault location detection through envelope analysis of

start-up current using Hilbert transform, Mechanical Systems and Signal Processing 2017; 93: 332–350. https://doi.org/10.1016/j.ymssp.2017.02.014.

5. Abd-El-Malek M, Abdelsalam A K, Hassan O E. Novel approach using Hilbert Transform for multiple broken rotor bars fault location detection for three phase induction motor, ISA Transactions 2018; 80: 439–457. https://doi.org/10.1016/j.isatra.2018.07.020.
6. Ali M Z, Shabbi M N, Liang X. Machine Learning-Based Fault Diagnosis for Single-and Multi-Faults in Induction Motors Using Measured Stator Currents and Vibration Signals, IEEE Transactions on Industry Applications 2019; 55(3): 2378–2391. https://doi.org/10.1109/TIA.2019.2895797.
7. Allal A, Khechekhouche A. Diagnosis of induction motor faults using the motor current normalized residual harmonic analysis method, International Journal of Electrical Power and Energy Systems 2022; 141: 108219. https://doi.org/10.1016/j.ijepes.2022.108219.
8. Zhang S, Wang B, Kanemaru M. Model-Based Analysis and Quantification of Bearing Faults in Induction Machines, IEEE Transactions on Industry Applications 2020; 56(3): 2158–2170. https://doi.org/10.1109/TIA.2020.2979383.
9. Gao Y, Liu X, Xiang J. FEM Simulation-Based Generative Adversarial Networks to Detect Bearing Faults, IEEE Transactions on Industrial Informatics 2020; 16(7): 4961–4971. https://doi.org/10.1109/TII.2020.2968370.
10. Lannoo J, Vanoost D, Peuteman J. Improved Air Gap Permeance Model to Characterise the Transient Behaviour of Electrical Machines Using Magnetic Equivalent Circuit Method, International Journal of Numerical Modelling: Electronic Networks, Devices and Fields 2020; 33(5): 2749. https://doi.org/10.1002/jnm.2749.
11. Gong X, Zhi Z, Feng K, Du W. Improved DCNN Based on Multi-Source Signals for Motor Compound Fault Diagnosis, Machines 2022; 10(4): 277. https://doi.org/10.3390/machines10040277.
12. Roy S S, Chatterjee S, Roy S. Accurate Detection of Bearing Faults Using Difference Visibility Graph and Bi-Directional Long Short-Term Memory Network Classifier, IEEE Transactions on Industry Applications 2022; 58(4): 4542–4551. https://doi.org/10.1109/TIA.2022.3167658.
13. Martinez-Herrera A L, Ferrucho-Alvarez E R, Ledesma-Carrillo L M, Mata-Chavez R I, Lopez-Ramirez M, Cabal-Yepez E. Multiple Fault Detection in Induction Motors through Homogeneity and Kurtosis Computation, Energies 2022; 15(4): 1541. https://doi.org/10.3390/en15041541.
14. Bautista-Morales M D R, Patiño-López L D. Acoustic Detection of Bearing Faults Through Fractional Harmonics Lock-in Amplification, Mechanical Systems and Signal Processing 2023; 185: 109740. https://doi.org/10.1016/j.ymssp.2022.109740.
15. Zhu Q Y, Lu J F, Wang X X, Wang H, Lu S L, De-Silva C W, Xia M. Real-Time Quality Inspection of Motor Rotor Using Cost-Effective Intelligent Edge System, IEEE Internet of Things Journal 2023; 10(8): 7393–7404. https://doi.org/10.1109/JIOT.2022.3228869.
16. Vu M H, Nguyen V Q, Tran T T, Pham V T, Lo M T. Few-Shot Bearing Fault Diagnosis Via Ensembling Transformer-Based Model With Mahalanobis Distance Metric Learning From Multiscale Features, IEEE Transactions on Instrumentation and Measurement 2024; 73. https://doi.org/10.1109/TIM.2024.3381270.
17. Dong X, Yuan J Y, Xiong L J, Niu G. Fault Detection of Interturn Short Circuit in Induction Motors Under Nonstationary Conditions and Unbalanced Supply Voltage, IEEE Transactions on Instrumentation and Measurement 2024; 73. https://doi.org/10.1109/TIM.2024.3403170.
18. Purbowaskito W, Lan C Y, Fuh K. Introducing Model-Based Residual Spectrum Analysis for a Practical Improvement in Induction Motors Fault Diagnosis, IEEE Transactions on Energy Conversion 2024; 39(3): 1958–1971. https://doi.org/10.1109/TEC.2024.3376684.
19. Song H, Yuan R, Lv Y, Pan H Y, Yang X K. Improved 2-D Multiscale Fractional Dispersion Entropy: A Novel Health Condition Indicator for Fault Diagnosis of Rolling Bearings, IEEE Sensors Journal 2024; 24(3): 3431–3444. https://doi.org/10.1109/JSEN.2023.3343399.
20. Gao J, Shang P. Analysis of complex time series based on EMD energy entropy plane, Nonlinear Dynamics 2019; 96(1): 465–482. https://doi.org/10.1007/s11071-019-04800-5.
21. Pickover C A. On the Use of Symmetrized Dot Patterns for the Visual Characterization of Speech Waveforms and Other Sampled Data, The Journal of the Acoustical Society of America 1986; 80(3): 955–960. https://doi.org/10.1121/1.393918.
22. Derosier B L, Normand M D, Peleg M. Effect of Lag on the Symmetrised Dot Pattern (SDP) Displays of the Mechanical Signatures of Crunchy Cereal Foods. Journal of the Science of Food and Agriculture 1997; 75(2): 173–178. https://doi.org/10.1002/(SICI)1097-0010(199710)75:2<173::AID-JSFA858>3.0.CO;2-9.